Pulsed Nd: YAG Laser Dissimilar Welding of Ti/Al_{3105} Alloys

Abeer A. Shehab[a,b], S.K. Sadrnezhaad[c,*], A.K. Mahmoud[a], M.J. Torkamany[d], A.H. Kokabi[c], M. Fakouri Hasanabadi [c]

[a]Department of Material Engineering, College of Eng., University of Diyala, Diyala, Iraq

[b]Institute of Laser for Postgraduate Studies, University of Baghdad, Baghdad, Iraq

[c]Department of Materials Science and Engineering, Sharif University of Technology Tehran, Iran

[d]Iranian National Center for Laser Science and Technology (INLC), Tehran, Iran

***Corresponding author**: sadrnezh@sharif.edu +989121303135

Abstract

Overlapped strips of titanium grade 2 and aluminum 3105-O alloy were welded together by an innovative spot-like pulse laser procedure. The tactile seam tracking on ring paths yielded reliable weld fit-up of 1 and 0.5 mm thickness strips. Since the welding parameters of Ti-Al were narrow, three welding speeds of 4, 5 and 6.67 $mm{\cdot}s^{-1}$ were chosen for the pretest conditions. The microstructural investigations showed that intermetallic compound Ti_3Al, formed in Ti-rich fusion zone. Cracks formed in the Al-rich fusion zone as a result of $TiAl_3$ precipitation. Dimple fracture occurred at 6.67 $mm{\cdot}s^{-1}$ welding speed. Longer mixing time at Ti-Al interface occurred at lower welding speeds of 4 and 5 $mm{\cdot}s^{-1}$, which led to the formation of thicker intermetallic compounds and more massive crack generation. It also increases the hardness of the fusion zone and results in brittle fracture type during the tensile test. The highest strength was achieved with a welding speed of 4 $mm{\cdot}s^{-1}$ which was a result of more massive weld nugget and lower porosity.

Keywords: welding, strip, joining, lasers, lapping, aluminum, titanium, keyhole

1. Introduction:

Research on welding of titanium to aluminum has been considered significant for aerospace, automotive and shipbuilding industries [1–6]. Due to low density, high strength, superior toughness, and resistance to corrosion, previous authors have defined any advancement in this field as substantial to the growth of new technologies [1,7]. The high ductility makes Al 3105-O an excellent candidate to replace aluminum 3003 that used in the airplane cabin fins which receive hot or cold fluid from carrying pipes made of titanium grade 2.

The difference in the lattice structure and thermophysical properties of Al and Ti makes their joining process a real challenge, especially by conventional fusion welding methods. From the Ti-Al equilibrium diagram, one can gather that Al does not allow dissolution of much Ti, where titanium can form a Ti-rich solid solution of up to ~12 atom% Al [8]. Negative enthalpies of dissolution [9] help fast fusion of the mixture; while various intermetallic compounds (IMCs) like $TiAl_{3.3}$, TiAl, Ti_5Al_{11}, Ti_9Al_{23}, and $Ti_{3.3}Al$ can also be formed [10]. Intermediate materials have introduced, however, a possible solution to surpass the IMCs problem in the dissimilar welding practices [11].

Laser welding of alloys provides many advantages over conventional techniques such as great precision, super speed, great flexibility, high quality and low distortion [12–20]. Majumdar et al. [9] have concluded that obtaining Al contents below 20 atom% in the Al-Ti mixing zone and crack free weld via the combination of any process parameters during Carbon Dioxide (CO_2) laser welding of Ti-6Al-4V and AlMg0.9Si is impossible. They have observed that sandwiching of Nb plate between Ti and Al sheets, keeps 11 atom% Al in the FZ and formation of TiNb solid solution with a crack-free joint.

Chen et al. [18] have reported that the formation of IMCs inside Ti weld can be suppressed by lowering the laser power or decreasing the welding speed during CO_2 laser welding in overlap titanium-on-aluminum configuration. Kreimeyer et al. [19] have reported that the thickness of IMCs mainly depends on the energy input per unit length. They obtained IMC thicknesses less than 2 μm in CO_2 laser welding where crack propagation from the Al HAZ towards IMCs resulted in ductile fracture of the weld. Tomashchuka et al. [20] studied the effect of beam energy and beam offset on the weld morphology, microstructure, and mechanical properties. They observed the formation of a wide contact interface (90-300 μm) rich in Al_3Ti phase when the laser beam is located at the center or AA5754 side. Maximal joint strength is obtained when shifting the laser beam to AA5754 side due to the formation of a thin interface (<20 μm) composed mostly by TiAl. Chelladurai et al. [21] have studied the effect of pulsed Nd: YAG laser energy on the disposition of conduction, transition, penetration, and keyhole. Grain refinement by rapid cooling and hard ceramic particles produced by in-situ reactions may also cause microhardness increase [22]. Chen et al. [23] have reported on the residual stress induction caused by the difference between thermal expansion coefficients of 5A06 Al and Ti–6Al–4V leading to crack initiation and its propagation within the reaction layer during the welding brazing process. They have expected that lamellas, cellular and club-shaped interfacial layers are responsible for enhancing the mechanical property of the joints by preventing the crack initiation and propagation.

Some authors have changed the length of the Al-Ti interface by changing joint configuration via making a groove [23] or a chamfer [24] on the welding materials. Vaidya et al. [24] have reported joint modification via chamfering of Ti-6Al-4V to the AA6056 alloy by the laser which reduced $TiAl_3$ formation. They observed the increase of fatigue crack propagation with the cooling rate which resulted in complete transgranular fracture of FZ next to the weld interface. From their results, one could conclude that grooving is more helpful than making a chamfer.

In the present study, a tactile seam tracking system is designed for pulse welding of titanium grade 2 to aluminum 3105-O alloy by a high-energy laser instrument. Increase the length of joining of very dissimilar material (Ti-Al) at the interface, via utilizing a ring weld path, assist the achievement of sufficient joint strength and results in efficient usage of the limited area allowable for welding maneuver. Effect of welding speed on microstructure and mechanical properties of the joint is discussed in the paper.

2. Materials and Methods

Commercial sheets of Ti (G2) and 3105-O Al were used for welding tests. The chemical composition of the materials was analyzed by using atomic absorption instrument GBC, model: Avanta PM, Australia. A SANTAM model STM-20, Universal Testing Machine was used to determine the base metal sheet mechanical properties according to the standard ASTM-E8, sub-size tensile specimen (Figure 1) by taking the average of three tests. The exact grade of the materials has been confirmed by comparing the experimentally determined chemical composition and mechanical properties with the standards Ref. [25]. Chemical compositions and properties of the materials used are given in Tables 1, 2 and 3.

The thickness of Ti (G2) was 1 mm and of Al 3105-O was 0.5 mm. Both metals were cut into 40×5 mm^2 rectangle strips. The surfaces of the strips were degreased by acetone, polished with emery papers, cleaned with 6-10 % NaOH alkaline solution for 5 min and then rinsed with tap water followed by 30 % HNO_3 + 3 % H_2SO_4 acid solution for 3 min. Ti strips were etched for 5 min with 20 % HNO_3+ 5 % HF acid solution and then wiped and rinsed with ethanol and tap water, ten min before welding test. The strips were overlapped for 5 mm and were welded in a circular path by overlapping repeated laser pulses, as shown in Figure 2.

Nd: YAG laser apparatus (Model IQL-10) with normal power of 400W produced standard square-shape pulses of 1–1000 Hz frequency, 2-20 ms duration and 0-40 J energy. The focal length of the focusing optical system was 75 mm which created spots of ~250 μm size. A movable XYZ table moved the clamping device under laser head of 0.05 mm positioning precision. Set up of the welding system was as demonstrated in Figure 2. A coaxial nozzle around the laser beam blew the shielding gas (argon of 99.999% purity) at the rate of 20 $L.min^{-1}$ to top of the weld line.

For tension tests, the cross-head speed of SANTAM testing machine was 5 $mm.min^{-1}$. Three measurements were done for each data point. After welding, the samples were wire-cut from near the welding zone. Grinding with abrasive silicon carbide papers of 600, 800, 1200, 2000 and 3000 $grain.in^{-2}$ and subsequent polishing of the samples with 3 different grain sizes of wet alumina powder on felt wheels were performed.

For microstructural examination of the weld zone, etching with fresh Kroll reagent was done for 30 s. The optical microscope, scanning electron microscope (SEM) and TESCAN MIRA 3 (Czech) equipped with energy dispersive X-ray spectrometry (EDS) inspected appearance, geometry, microstructure and fracture zone of the joints. To investigate phase formation at fracture surfaces, x-ray diffraction (XRD) with PAN, Model X'Pertequipped with PIXcel detector and X'Pert high score plus (V.3) software, was used. The metal target was Cu; step size was 2 θ; diffraction angle was 15 at the start and 80º at the end. BUEHLER model MMT1, USA determined Vickers micro-hardness values. Loading force was 25 g which was applied for 25 s. Average of three measurements was recorded for different locations: BM, HAZ, and FZ of each side of the joints.

3. Results and Discussion

Seam welding procedure of ring path performed with pulse lasering spot-method provided the premium solution to the problem of high-quality Ti-Al joint achievement. Applying conventional laser welding with all combinations of pulse duration and peak power, whether single or multi-pulse and at the same or different positions did not give enough strength in the welded couple so that the sample could not withstand the pull-out force for its removal from the clamping device. However, overlapping pulses of ring path resulted in a shear strength of around 10 MPa which depended on the welding speed.

Due to its significant effect on the amount of heat input and the interaction period between the heat source (laser beam) and the weld metal, variation of welding speed had more significant effect on the bead depth than its width [26,27]. The welding speed has thus a significant effect on the strength of the weld. Another essential factor of seam welding was pulse overlapping, which strongly affected the weld quality by efficient heating and continuous penetration of the substances. The variation of the welding speed affected pulse overlapping and uniform pool formation. Based on pretest experiments, the welding parameters chosen for the work were as listed in Table 4.

3.1 Weld Appearance

Figure 3 shows top (Ti) view of the welded samples 1 to 3. The appearance of the surfaces shows the effect of the welding speed on weld zones of the samples. Figure 4 depicts the effect of the speed of welding on the diameter of the weld zone viewed from the top. It shows that lower speed results in a larger weld zone. This effect attributes to the higher energy input due to the longer beam incidence which leads to a broader base-metal pool and a greater weld diameter (3.4 mm for 4 $mm.s^{-1}$ welding speed) (see Figure 3a). Getting a perfect joint between the welded partners requires a reasonable level of pulse overlapping, where overlapping of the succeeding pulses leads to a continuous seam weld as is observable in Figure 5a.

Overlapping factor (O_f) is defined as [28]:

$$O_f(\%) = \frac{1-(V/f)}{S+(V\times T)} \times 100 \qquad (1)$$

Where V is the welding speed, f is laser frequency, T is pulse duration, and S refers to the laser spot size on work-piece that was 0.8 mm throughout our tests. Figure 5 depicts the effect of laser beam overlapping on surface area and keyhole depth. It can be seen that at the welding speed of 6.67 $mm.s^{-1}$ (60% overlapping), the distance between the keyhole roots is longer than the other welds being inversely proportional to the overlapping factor Q_f.

By insertion of the test values, i.e., pulse frequency = 20 Hz, T= 6 ms and S = 0.8 mm into Eq. 1, the respective O_f factor became 60, 70 and 76 % for our welding speeds of 6.67, 5 and 4 $mm.s^{-1}$. Eq. 2 gives the average energy input per unit area (Ea) [29]:

$$E_a = \frac{E_{pulse}\times pulse\ frequency}{\frac{S}{2}} \times V \qquad (2)$$

Decreasing the welding speed (i.e., increasing the overlapping factor O_f) leads to a significant energy effect from the earlier pulse and the severe interaction of the next laser pulse with the metal which results in the change of the conical appearance of the welding zone (keyhole shape) to a cylindrical one. This change results in more efficient energy absorption and more ejection of energy through the generated keyhole ending up with a larger melt volume. This hypothesized mechanism also agrees well with the results of the earlier investigations [28–32].

Experimental results show that a welding speed of 4 $mm.s^{-1}$ (76% overlapping) results in a deeper penetration(342 μm) than the higher welding speed of 6.67 $mm.s^{-1}$ (60% overlapping) (184 μm). This is due to the input of a stronger focal energy at the lower speed which is in agreement with the mechanism described by the previous authors [18,33]. In last pulse region (end spot of the ring welding path), there are three pulses which collide to the same place before the laser power-supply turns off and the moving head wholly stops. A big circular dip forms at this position at all three speeds, as seen in Figure 3.

Because of higher energy absorption and penetration continuity, overlapping has a powerful influence on the welding efficiency, as indicated by previous researchers [34]. Figure 6 shows the shape of the fused area at the bottom of the Ti strip for different overlapping pulses (O_f) of (a) 76, (b) 70 and (c) 60%. Incomplete fusion appears in some zones of the strip with 60 % overlapping occurrence. The porosities that form in the 60 % O_f sample do not allow energy response for the formation of a continuous complete weld. Multiple pulses of higher overlapping at lower welding speed can improve the joint, as is understandable from Figure 6 a and c. Porosity decrease due to the lowering of the welding speed indicates higher heat input rate which induces an upward flow of the melt to give a chance to the gas bubbles to ascend through the molten pool for their eventual egress, as observed in Figure 6. This mechanism seems to prove a narrow window for the influence of the welding parameters.

Figure 7 presents images of the cross Sections 1, 2 and 3 of the weld zone (labeled in Figure 3). This figure shows that penetration depth (for the ordinary overlapped pulses) increases with lowering of the welding speed. This increase is due to the higher energy input that leads to a deeper melt pool which agrees well with results of a previous investigation [18]. Figure 7 shows small porosities near fusion boundaries. These porosities attribute to gases which are soluble in the liquid melt but insoluble in the solid phase. High solidification rate of the molten pool does not allow the entrapped gases to escape. Initial sources of gas are interfacial and shielding moisture. Effects of both regular and last pulses on the geometry of the weld bead are seen in Figure 7. Due to the extensive energy input of the last three pulses, broader and deeper weld pool forms at the final stage of our circular welding process.

3.2 Weld Microstructure

Figure 8 illustrates the microstructure of sample 1. The microstructure of Ti (G2) base-metal has equiaxed α grains of uniform size. Energy input during welding generates coarse equiaxed grains in the HAZ and serrated α grains in some areas of the FZ where heat transfer is along transversal and axial directions. Presence of fine equiaxed grains in the HAZ region next to the molten boundary is due to rapid cooling of the weld metal.

The high cooling rate of more than 10^4 $K.s^{-1}$ during laser welding [12] is responsible for the formation of the martensite-like structure seen in Figure 8b. This process modifies the shape and size of the grains in the FZ of Figure 8a. Ti-α grains in FZ region (bigger than the base-metal) are observable in this figure.

Figure 8c shows cellular grains grown at the boundary between Al BM and Ti-rich FZ, which are high rate directional heat ejection towards the Al BM. The high thermal conductivity of Al results in rapid heat transfer and fast cooling in this region.

All areas next to the connection interface consist of columnar grains that are also parallel to the cooling direction. Grains become smaller from Al alloy towards the connection interface owing to the cooling rate enhancement in this direction.

At higher welding speeds of 5 and 6.67 $mm.s^{-1}$, there is no time for full melt-down of titanium. Ti-Ai inter-diffusion at these speeds is also slow due to energy shortage and lack of time. Rapid cooling, thus, results in the creation of aluminum-rich IMCs ($TiAl_3$ and/or $TiAl_2$) near Al FZ, consistent with the equilibrium phase diagram [8]. Susceptibility to solidification cracking of the weld near Al FZ, hence, increases at higher welding rates. Figure 9a shows part of Al-Ti interface for 5 $mm.s^{-1}$ welding speed. Cracks are observable near the Al side of the connection. EDS point scan of point C (see Figure 9b) indicates the formation of $TiAl_3$ (22 atom% Ti and 77 atom% Al) in the Al FZ region. Partial melt-down of Ti is expected at higher welding speeds near Al fusion zone.

Local hardness increases of the connection region are due to high values of modulus of elasticity of $TiAl_3$ in addition to the residual stresses which exist in the connection [28]. Due to the large difference between thermal conductivity of the Al alloy (173 $W.m.K^{-1}$) and Ti (16.4 $W.m.K^{-1}$) [24] and low ductility of $TiAl_3$, the high thermal gradient existing across the connection between the fusion zone and the Al re-solidified alloy can lead to high residual stress near the connection. Since $TiAl_3$ cannot bear this thermal shock, cracks form in the connection region of the welded samples [9].

3.3 Point Scan Pattern

Figure 10 shows microstructure of zone A of Figure 7a and its adjacent regions. Figure 10a shows a high magnification SEM image of zone A. Figure 10 b, c, and d shows the respective EDS results of points A, B, and C of part (a). Table 5 presents the analysis of these points. It is seen that the weld zone has mainly intermetallic phase Ti_3Al (at Ti side), $TiAl_3$ (at Ti-Al interface) and Al in FZ near the Ti-Al interface.

Figure 11 shows high magnification SEM images of point C for welding speeds of 4 and 6.67 $mm.s^{-1}$. EDS analyses show the disposition of $TiAl_3$ in both cases. Crack formation occurs at the welding speed of 4 $mm.s^{-1}$ (Figure 11b), while not observable at the speed of 6.67 $mm.s^{-1}$ (Figure 11a). Aforementioned could have resulted from considerable heat input, low weld speed, small cooling rate and prolonged Ti-Al mixing which results in enormous amounts of IMCs ($TiAl_3$) at $mm.s^{-1}$. This compound is very brittle and unable to withstand the generated thermal shock and thus cracks, as observed in Figure 11 b.

3.4 Mechanical Behavior

Mechanical properties of the joint are defined in terms of both tensile or shear strengths and microhardness.

3.4.1 Shear Strength of the Joint

Table 6 represents the shear force and length extension of the samples at various welding speeds. Upshot effect of the laser pulses shows 60 % overlap at 6.67 $mm.s^{-1}$, 70 % at 5 and 76 % at 4 $mm.s^{-1}$. At higher welding speed of 6.67 $mm.s^{-1}$, the greatest shear force is lower (244 N) due to the smaller O_f; while at the lower welding speed of 4 $mm.s^{-1}$, the greatest shear force is higher (264 N). Incomplete fusion at the areas located between the overlapped pulses at the bottom of the Ti sheet at lower overlap percentages is the cause of this effect (see Figure 6c). Nonfused areas combined with residual stresses of shear loads can cause crack initiation [23]. Porosities present at the Ti-Al interface (see Figures 6 c and 7c) can also have a negative effect on the joint strength.

Figure 12 a, and d presents the optical and SEM images of the samples fractured at the welding speed of 6.67 $mm.s^{-1}$. It shows that fracture has started from the welding zone. This start has been due to the de-bonding of the unfinished fusion areas together with porosity effects. SEM images of the fractured surfaces show a honeycomb-like structure that indicates ductile fracture [19]. That is due to the smaller thickness of IMCs formed at the Ti-Al interface at the welding speed of 6.67 $mm.s^{-1}$ (high cooling rate) where less time is available for mixing of Ti with Al. Higher shear force (264 N) at the lower welding speed of 4 $mm.s^{-1}$ leads to deeper penetration of titanium into aluminum and larger width of joining due to higher heat input. The wider melted area (3.77 mm^2) at Ti-Al interface (average of three measurements) besides lower porosity levels of sample 3 gives the higher value of 264 N shear force with longer extension during the tensile test (see Table 6, Figure 6a).

The joint strength in lap joint design mainly depends on the melted area of the connection and the strength of the welded sheets [35,36]. Dividing the shear force (264 N) by surface area ($3.77mm^2$) gives the shear stress at the interface. The result is 70 MPa shear stress.

Figure 12 b, and c presents the optical images of the fractured samples 2 and 3. Images indicate breaking of the sample from Al FZ that is very close to the Ti-Al interface. As a result, one can infer that the cracks form in the IMC zone. That is due to the high heat input (see Figures 9 a, 11 b) which agrees with the literature [37]. SEM images of the fractured surfaces of the samples 2 and 3

are also presented in Figures12 (e and f). Figure 12 also shows locations of cleavage fracture. They indicate a brittle fracture [38].

X-ray diffraction (XRD) patterns of the fracture surface of sample 2 (welding speed: 5 $mm.s^{-1}$) of Figure 12 b is given in Figure 13. The small XRD peaks belonging to $TiAl_3$ (Figure 12 e) show IMCs $TiAl_3$ formation.

Figure 14 compares the values of (1) joint shear stress at the welding speed of 4 $mm.s^{-1}$ (76 % pulses overlap), (2) aluminum base-metal shear stress and (3) aluminum base-metal tensile stress. In dissimilar metals joint, it is more logical to compare the value of the shear stress of the joint (70MPa) with the shear stress of the lower strength base-metal, i.e., aluminum (82MPa). Joint shear strength as much as 85 % with respect to the base-metal is thus obtained.

3.4.2 Microhardness of the Joint

Vickers microhardness numbers (average of three measurements) of locations BM, HAZ, and FZ of the welded samples are marked in Figure 15. In the Ti side, the microhardness increases from Ti HAZ towards the FZ region. A drastic difference between Ti BM (125 HV) with the Ti FZ (317 HV) is also observed. Acicular α-martensite which forms due to thermal-cycling by the laser heat and next quench seems responsible for this difference, as also stated in [12]. The hardening effect observed in the Ti-Al dissimilar weld interface attributes to the IMCs formed at the hardened locations, as observed in Figure 15. It is also observed that the thickness of the IMCs changes with the welding speed. Different IMCs form at different cooling rates and times from the beginning of Ti-Al mixing. However, the increase in IMCs thickness that relates to decreasing of the welding speed, results in the joint hardness increase as seen from Figure 15 a, b, and c, where 412, 464 and 572 HV represent the maximum hardness values at Ti-Al mixing zone (MZ) respectively, thus dimple fracture was observed in sample 1 (Figure 12 d), while brittle cleavage occurred in samples 2 and 3 (Figures12 e and 12 f)

In the aluminum side of the connection, there is an increase in microhardness values from Al HAZ towards FZ region. The hardness of aluminum at FZ is higher than at Al BM. The higher hardness is because of higher grain growth and coarsening at lower cooling rates of Al BM as compared to the Al at FZ. The resulted increase in hardness of the Al at FZ as compared to the corresponding Al at BM (45HV) is thus logically due to the grain refinement which results from the high cooling rate of the laser-welded region.

4. Conclusions

Nd: YAG pulsed laser welding of dissimilar 1 mm thick titanium grade 2 strip and 0.5 mm thick aluminum 3105-O alloy belt showed that:

1. The specific spot welding procedure carried out during the present work was an efficient method for making a joint of very different materials, such as Ti-Al joint over the limited area allowable for welding.

2. Intermetallic compounds (IMCs) Ti_3Al was formed in Ti fusion zone (FZ) near the connection. Precipitation of $TiAl_3$ IMCs in Al FZ near the connection resulted in cracks formation.

3. Longer mixing time at lower welding speed leads to the formation of thicker IMCs, initiation of more cracks and the increase of hardness at the Ti-Al joint.

4. Welding speeds of 5 and 6.67 $mm.s^{-1}$ do not give desirable results due to the diminution of heat input and narrowing of the melt pool. Welding speed of 4 $mm.s^{-1}$ leads to larger width of joining of titanium into aluminum with lower porosity. Joint strength rose up to 85 % of the base aluminum alloy.

5. Acknowledgments

The authors would like to thank co-operation of the Institute of Laser for Postgraduate Studies, University of Baghdad, Sharif University of Technology, Iran National Science Foundation and Iranian National Center for Laser Science and Technology for their help and support in doing this work.

6. References

1. Möller, F., Grden, M., Thomy, C., and Vollertsen, F., "Combined Laser Beam Welding and Brazing Process for Aluminium Titanium Hybrid Structures", *Phys. Procedia*, **12**(PART 1), pp. 215–223 (2011).
2. Zhu, Z., Lee, K. Y., and Wang, X., "Ultrasonic welding of dissimilar metals, AA6061 and Ti6Al4V", *Int. J. Adv. Manuf. Technol.*, **59**(5–8), pp. 569–574 (2012).
3. Sohn, W. H., Bong, H. H., and Hong, S. H., "Microstructure and bonding mechanism of Al/Ti bonded joint using Al–10Si–1Mg filler metal", *Mater. Sci. Eng. A*, **355**(1–2), pp. 231–240 (2003).
4. Kahraman, N., Gulenc, B., and Findik, F., "Corrosion and mechanical-microstructural aspects of dissimilar joints of Ti-6Al-4V and Al plates", *Int. J. Impact Eng.*, **34**(8), pp. 1423–1432 (2007).
5. Cao, R., Sun, J. H., and Chen, J. H., "Mechanisms of joining aluminium A6061-T6 and titanium Ti–6Al–4V alloys by cold metal transfer technology", *Sci. Technol. Weld. Join.*, **18**(5), pp. 425–433 (2013).
6. Cao, X., Wallace, W., Immarigeon, J.-P., and Poon, C., "Research and Progress in Laser Welding of Wrought Aluminum Alloys. II. Metallurgical Microstructures, Defects, and Mechanical Properties", *Mater. Manuf. Process.*, **18**(1), pp. 23–49 (2003).
7. Costa, A., Miranda, R., Quintino, L., and Yapp, D., "Analysis of Beam Material Interaction in

Welding of Titanium with Fiber Lasers", *Mater. Manuf. Process.*, **22**(7–8), pp. 798–803 (2007).

8. Das, S., "The Al-O-Ti (Aluminum-oxygen-titanium) system", *J. Phase Equilibria*, **23**(6), pp. 525–536 (2002).
9. MAJUMDAR, B., GALUN, R., WEISHEIT, A., and MORDIKE, B. L., "Formation of a crack-free joint between Ti alloy and Al alloy by using a high-power CO2 laser", *J. Mater. Sci.*, **32**(23), pp. 6191–6200 (1997).
10. Wei, S., Li, Y., Wang, J., and Liu, K., "Use of welding-brazing technology on microstructural development of titanium/aluminum dissimilar joints", *Mater. Manuf. Process.*, **29**(8), pp. 961–968 (2014).
11. Mitelea, I., Groza, C., and Craciunescu, C. M., "Pulsed laser processing of dissimilar Ti-6Al-4V and X5CrNi18-10 joints", *Mater. Manuf. Process.*, **29**(8), pp. 975–979 (2014).
12. Katayama, S., *Handbook of Laser Welding Technologies*, 1st Edn., Wood Head Publishing, Cambridge (2013).
13. Pascu, A., Stanciu, E. M., Voiculescu, I., Țierean, M. H., Roată, I. C., and Ocaña, J. L., "Chemical and Mechanical Characterization of AISI 304 and AISI 1010 Laser Welding", *Mater. Manuf. Process.*, **31**(3), pp. 311–318 (2016).
14. Subashini, L., Prabhakar, K. V. P., Gundakaram, R. C., Ghosh, S., and Padmanabham, G., "Single pass laser-arc hybrid welding of maraging steel thick sections", *Mater. Manuf. Process.*, **31**(16), pp. 2186–2198 (2016).
15. Mirshekari, G. R., Saatchi, A., Kermanpur, A., and Sadrnezhaad, S. K., "Effect of Post Weld Heat Treatment on Mechanical and Corrosion Behaviors of NiTi and Stainless Steel Laser-Welded Wires", *J. Mater. Eng. Perform.*, **25**(6), pp. 2395–2402 (2016).
16. Mirshekari, G. R., Kermanpur, A., Saatchi, A., Sadrnezhaad, S. K., and Soleymani, A. P., "Microstructure, cyclic deformation and corrosion behavior of laser welded NiTi shape memory wires", *J. Mater. Eng. Perform.*, **24**(9), pp. 3356–3364 (2015).
17. Mirshekari, G. R., Saatchi, A., Kermanpur, A., and Sadrnezhaad, S. K., "Laser welding of NiTi shape memory alloy: Comparison of the similar and dissimilar joints to AISI 304 stainless steel", *Opt. Laser Technol.*, **54**, pp. 151–158 (2013).
18. Chen, S., Yang, D., Li, M., Zhang, Y., Huang, J., Yang, J., and Zhao, X., "Laser penetration welding of an overlap titanium-on-aluminum configuration", *Int. J. Adv. Manuf. Technol.*, **87**(9–12), pp. 3069–3079 (2016).
19. Kreimeyer, M., Wagner, F., and Vollertsen, F., "Laser processing of aluminum–titanium-tailored blanks", *Opt. Lasers Eng.*, **43**(9), pp. 1021–1035 (2005).
20. Tomashchuk, I., Sallamand, P., Cicala, E., Peyre, P., and Grevey, D., "Direct keyhole laser welding of aluminum alloy AA5754 to titanium alloy Ti6Al4V", *J. Mater. Process. Technol.*, **217**, pp. 96–104 (2015).

21. Chelladurai, A. M., Gopal, K. A., Murugan, S., Venugopal, S., and Jayakumar, T., "Energy Transfer Modes in Pulsed Laser Seam Welding", *Mater. Manuf. Process.*, **30**(2), pp. 162–168 (2015).
22. Sahu, J. K., Sahoo, C. K., and Masanta, M., "In-Situ TiB 2 –TiC–Al 2 O 3 Composite Coating on Aluminum by Laser Surface Modification", *Mater. Manuf. Process.*, **30**(6), pp. 736–742 (2015).
23. Chen, Y., Chen, S., and Li, L., "Influence of interfacial reaction layer morphologies on crack initiation and propagation in Ti/Al joint by laser welding–brazing", *Mater. Des.*, **31**(1), pp. 227–233 (2010).
24. Vaidya, W. V., Horstmann, M., Ventzke, V., Petrovski, B., Koçak, M., Kocik, R., and Tempus, G., "Improving interfacial properties of a laser beam welded dissimilar joint of aluminium AA6056 and titanium Ti6Al4V for aeronautical applications", *J. Mater. Sci.*, **45**(22), pp. 6242–6254 (2010).
25. *ASM Handbook Volume 2: Properties and Selection: Nonferrous Alloys and Special-Purpose Materials*, ASM International, Geauga County, Ohio, USA (1990).
26. Tadamalle, A. P., Reddy, Y. P., and Ramjee, E., "Influence of laser welding process parameters on weld pool geometry and duty cycle", *Adv. Prod. Eng. Manag.*, **8**(1), pp. 52–60 (2013).
27. Azadi Moghaddam, M., Golmezerji, R., and Kolahan, F., "Simultaneous optimization of joint edge geometry and process parameters in gas metal arc welding using integrated ANN-PSO approach", *Sci. Iran. B*, **24**(1), pp. 260–273 (2017).
28. Torkamany, M. J., Malek Ghaini, F., and Poursalehi, R., "Dissimilar pulsed Nd:YAG laser welding of pure niobium to Ti–6Al–4V", *Mater. Des.*, **53**, pp. 915–920 (2014).
29. Torkamany, M. J., Tahamtan, S., and Sabbaghzadeh, J., "Dissimilar welding of carbon steel to 5754 aluminum alloy by Nd:YAG pulsed laser", *Mater. Des.*, **31**(1), pp. 458–465 (2010).
30. Tzeng, Y.-F., "Process Characterisation of Pulsed Nd:YAG Laser Seam Welding", *Int. J. Adv. Manuf. Technol.*, **16**(1), pp. 10–18 (2000).
31. Torkamany, M. J., Sabbaghzadeh, J., and Hamedi, M. J., "Effect of laser welding mode on the microstructure and mechanical performance of dissimilar laser spot welds between low carbon and austenitic stainless steels", *Mater. Des.*, **34**, pp. 666–672 (2012).
32. Kim, T., Ha, K. H., and Chu, C. N., "Effects of material combination on laser beam drilling of a metal foil using a cover plate", *Mater. Manuf. Process.*, **32**(6), pp. 631–637 (2017).
33. Kalaiselvan, K., Elango, A., and Nagarajan, N., "Studies on weldment structure in Ti/Al dissimilar metal joints using Laser beam welding", *K. Kalaiselvan, A. Elango, NM. Nagarajan*, **21**(2) (2016).
34. Torkamany, M. J., Hamedi, M. J., Malek, F., and Sabbaghzadeh, J., "The effect of process parameters on keyhole welding with a 400 W Nd : YAG pulsed laser", *J. Phys. D. Appl.*

Phys., **39**(21), pp. 4563–4567 (2006).

35. Ion, J. C., *Laser Processing of Engineering Materials: Principles, Procedure and Industrial Application*, Elsevier, Oxford, England (2005).
36. Ready, J. F., Farson, D. F., and Feeley, T., *LIA Handbook of Laser Materials Processing*, Springer-Verlag Berlin Heidelberg, Heidelberg, Germany (2001).
37. Chen, S. H., Li, L. Q., and Chen, Y. B., "Interfacial reaction mode and its influence on tensile strength in laser joining Al alloy to Ti alloy", *Mater. Sci. Technol.*, **26**(2), pp. 230–235 (2010).
38. Chen, D.-C., Chang, D.-Y., Chen, F.-H., and Kuo, T.-Y., "Application of Ductile Fracture Criterion for Tensile Test of Zirconium Alloy 702", *Sci. Iran.*, **0**(0), pp. 0–0 (2018).

Abeer A. Shehab received his BA, in Mechanical Engineering from Baghdad University (2000) and Higher Diploma in Mechanical Engineering from Middle Technical University of Baghdad (2008) and his MA (2011) and Ph.D. (2015) from Baghdad University, Institute of Laser for Postgraduate Studies. During 2014, he was on a research mission at the Sharif University of Technology under Prof. S.K. Sadrnezhaad supervision. He spent six years as a faculty member at the University of Diyala, College of Engineering, Mechanical Engineering Department; then he moved to the Material Engineering Department as a lecturer for welding and casting processes in 2017. His primary interest remains in the field of welding laser material processing (laser welding, laser drilling, laser surface treatments, and laser cutting).

S.K. Sadrnezhaad is a distinguished professor at the Department of Materials Science and Engineering of the Sharif University of Technology. His current interest is in the emerging bio-nano fields of the materials science and engineering discipline. His Ph.D. dates back to 1979 from the Massachusetts Institute of Technology. So far, he has authored and coauthored five books, more than 600 technical papers, and more than 60 patents.

Adel K. Mahmoud is Full Professor in the Metallurgical & Mechanical Engineering at the Department of Material Engineering, College of Engineering, the University of Diyala in Iraq. He received B.Sc., M.Sc. and Ph.D. degrees in the Metallurgical Engineering from the University of Technology of Baghdad in Iraq. Dr. Adel has more than forty papers published in the Proceedings of International Conferences and Journals in fields of the Materials Engineering, Laser Welding of Engineering Materials, and Nanotechnology. His current research lies in the areas of Surface Engineering, Laser Processing of Engineering Materials, and Nanomaterials.

Mohammad Javad Torkamany has a BSc in Applied Physics and an MSc in Atomic and Molecular Physics from the University of Isfahan; and a Ph.D. in Material Engineering from Tarbiat Modares University that he obtained in 2015. Dr. Torkamany has worked as a researcher in the field of High Power Laser Welding at the Lulea University of Technology of Sweden. Currently, he is a faculty member of the Iranian National Center for Laser Science and Technology (INLC) working on laser material processing especially pulsed laser

welding, nanoparticle production by pulsed laser ablation in liquids, nonlinear optical properties of laser-synthesized nano and dissimilar laser welding.

Amir Hossein Kokabi received his B.Sc. in Industrial Metallurgy from the Sharif University of Technology in 1970. He was directly accepted in Ph.D. at University of Strathclyde and received his degree in Welding Metallurgy in 1980. Prof Kokabi is a faculty member of the Sharif University of Technology. He has done extensive work and has also written several books in the field of metals, ceramics and polymers joining and also material processing using welding technologies.

Masood Fakouri Hasanabadi graduated with a Bachelor in Materials Engineering from the Ferdowsi University of Mashhad in 2011, and an M.Sc. and a Ph.D. in welding from the Sharif University of Technology in 2013 and 2018. He worked as a researcher at the Institute of Energy and Climate Research of Forschungszentrum Jülich and also Renewable Energy Department of Niroo Research Institute for several months from 2016 to 2018. He is currently active in pursuing research at welding and ceramic-metal joining.

List of Tables

Figure Captions

Figure 3. Appearance of the top surface of Ti-Al laser welded couple with various welding speeds: (a) 4, (b) 5 and (c) 6.67 $mm.s^{-1}$.

Figure 4. Diameter of the weld zone (mm) vs. (a) laser welding speed ($mm.s^{-1}$) and (b) energy input ($J.mm^{-2}$).

Figure 5. Surface and depth of the keyhole affected by laser beam overlapping (Q_f) of: (a) 76%, (b) 70% and (c) 60%.

Figure 6. Images of fused areas at bottom of Ti sheet for different overlapping factor (O_f) values: (a) 76%, (b) 70% and (c) 60%.

Figure 7. Cross sections of the weld strips highlighted in Figure 3: (a) Section 1, (b) Section 2 and (c) Section 3.

Figure 8. Microstructure of sample 3 (V = 6.67 $mm.s^{-1}$); (a) serrated α grains in fusion zone of a single pulse, (b) acicular ά martensite in Ti fusion zone, and (c) Al base-metal/fusion zone interface.

Figure 9. Cracks near the Ti-Al interface at welding speed of 5 $mm.s^{-1}$: (a) SEM image and (b) EDS result.

Figure 10. Microstructures of zone A of Figure 7a and its adjacent regions: (a) SEM image for zone A, and (b, c and d) EDS pattern of points A, B, and C of part (a), respectively.

Figure 11. SEM image nearby the point C at the welding speed of: (a) 6.67 and (b) 4 $mm.s^{-1}$.

Figure 12. Optical (a, b, and c) and SEM (d, e, and f) images of the samples fractured under shear load at welding speed of: (a,d) 6.67, (b,e) 5, and (c,f) 4 $mm.s^{-1}$.

Figure 13. XRD patterns at the fracture interface of Ti shown in Figure 12e.

Figure 14. Values of: (1) the shear stress for the joint welded at 4 $mm.s^{-1}$ (76% pulses overlap), (2) the shear stress for the Al base-metal, and (3) the tensile stress for Al base-metal.

Figure 15. Base-metal (BM), Fusion Zone (FZ) and Mixing Zone (MZ) microhardness measurement locations on the Ti-Al couple welded at the speed of: (a) 6.76, (b) 5 and (c) 4 $mm.s^{-1}$.

Table 1. Chemical composition of the raw materials in wt%.

Alloy	C	Mn	Cr	Zn	O	Mg	Cu	Fe	Al	Ti
Al 3105-O	-	0.500	0.008	0.060	-	0.500	0.090	0.610	Bal.	-
Ti (G2)	0.080	-	-	-	0.200	-	-	0.080	-	Bal.

Table 2. Mechanical properties of the raw materials.

Alloy	Yield stress (MPa)	Ultimate tensile strength (MPa)	Elongation (%)	Hardness (HV)
Al 3105-O	55	122	24	45
Ti (G2)	275	344	28	125

Table 3. Thermophysical properties of the materials used [22].

Alloy	Thermal conductivity ($W.m^{-1}.K^{-1}$)	Density ($g.cm^{-3}$)	Melting point (^oC)	Thermal expansion coefficient ($K^{-1}.\mu m.m^{-1}$)
Al 3105-O	173.0	2.7	660.0	23.6
Ti (G2)	16.4	4.5	1665.0	9.4

Table 4. Values selected for the best welding performance.

Sample No.	Pulse energy E_{pulse} (J)	Pulse duration T (ms)	Welding speed V ($mm.s^{-1}$)	Peak power (kW)	Argon gas flow rate ($L.min^{-1}$)	Pulse frequency f (HZ)	Overlapping factor (%)	Average energy input ($J.mm^{-2}$)
1	11	6	4.00	1.83	20	20	76	137.5
2	11	6	5.00	1.83	20	20	70	110.0
3	11	6	6.67	1.83	20	20	60	82.4

Table 5. Weight and atomic percentages of Al and Ti at points A, B, and C of Figure 10a.

Point	Ti		Al		Ti_xAl_y	Comment
	wt. %	atom%	wt%	atom%		
A	89.3	82.6	10.3	16.9	Ti_3Al	Mixed (αTi + IMCs Ti_3Al)
B	69	56	29.9	43	TiAl	IMCs
C	7.5	4	89.8	93	$TiAl_3$	IMCs

Table 6. Effect of welding speed on mechanical properties of the joint.

Welding speed ($mm.s^{-1}$)	Shear force at the yielding point (N)	Shear strength (N)	Length extension (mm)
4.00	30	264	1.66
5.00	39	256	1.45
6.67	62	244	1.05

Figure 1. SANTAM, universal testing machine and Al sub size tensile specimen.

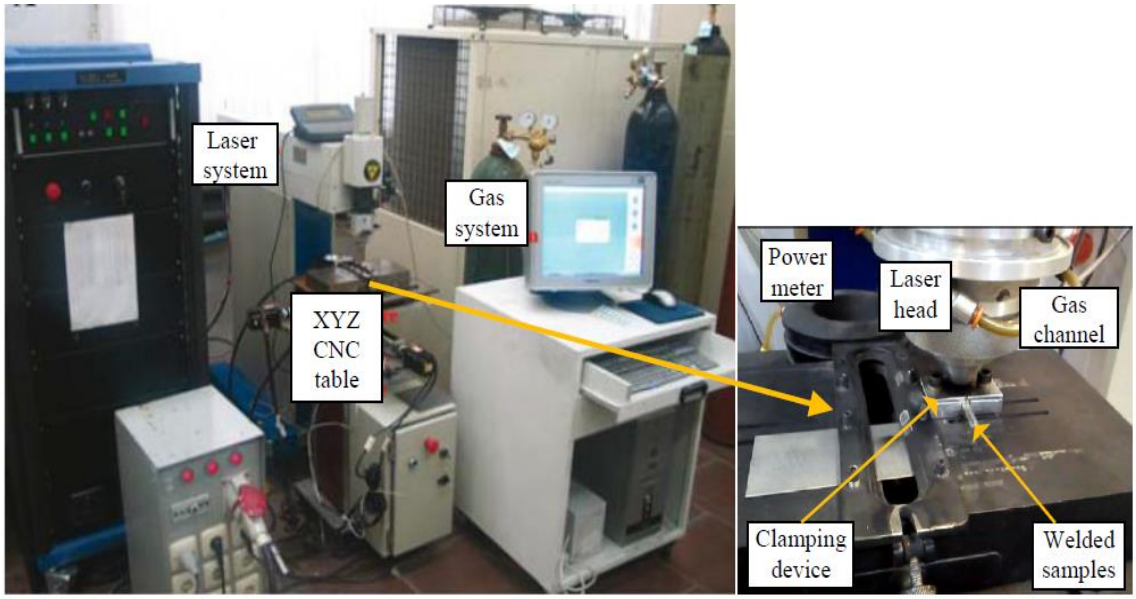

(a)

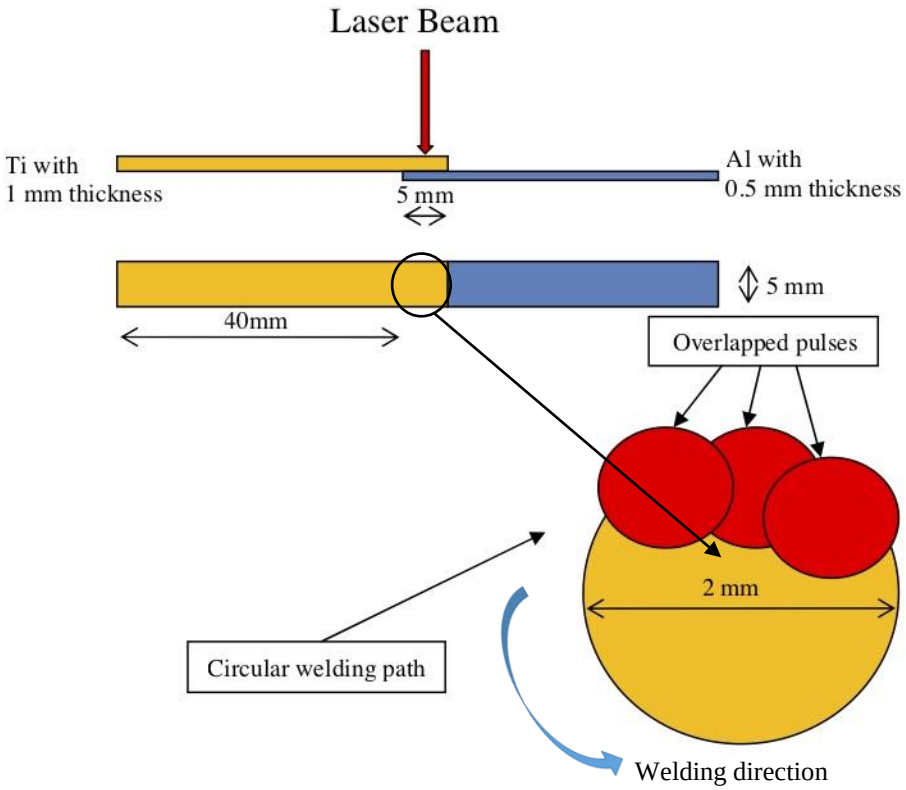

(b)

Figure 2. Laser welding of Ti-Al strips: (a) equipment and (b) setup geometry.

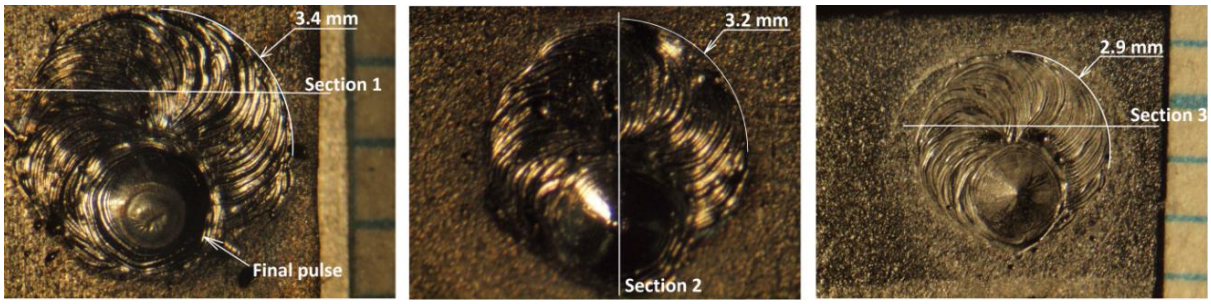

(a) (b) (c)

Figure 3. Appearance of the top surface of Ti-Al laser welded couple with various welding speeds: (a) 4, (b) 5 and (c) 6.67 mm.s^{-1}.

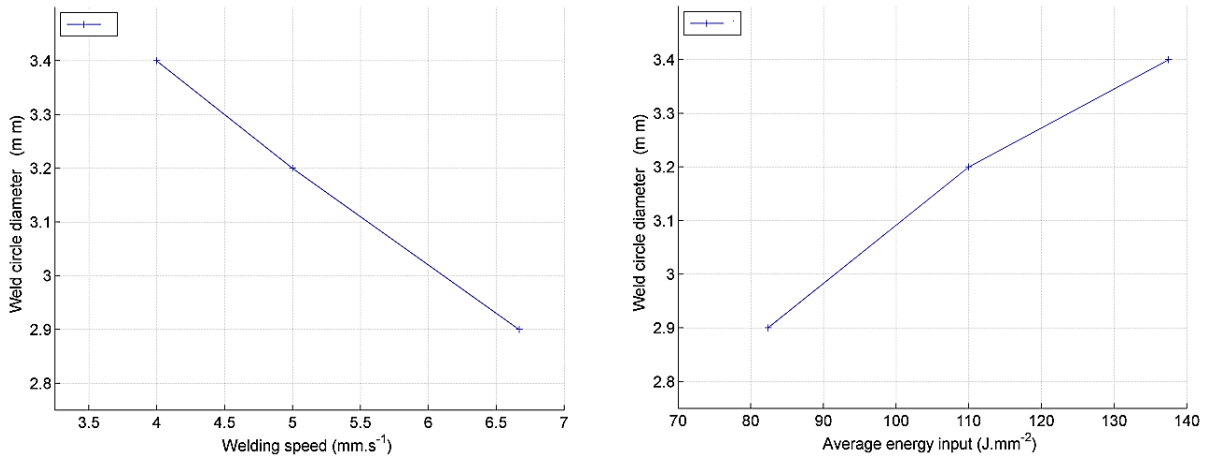

(a) (b)

Figure 4. Diameter of the weld zone (mm) vs. (a) laser welding speed (mm.s^{-1}) and (b) energy input (J.mm^{-2}).

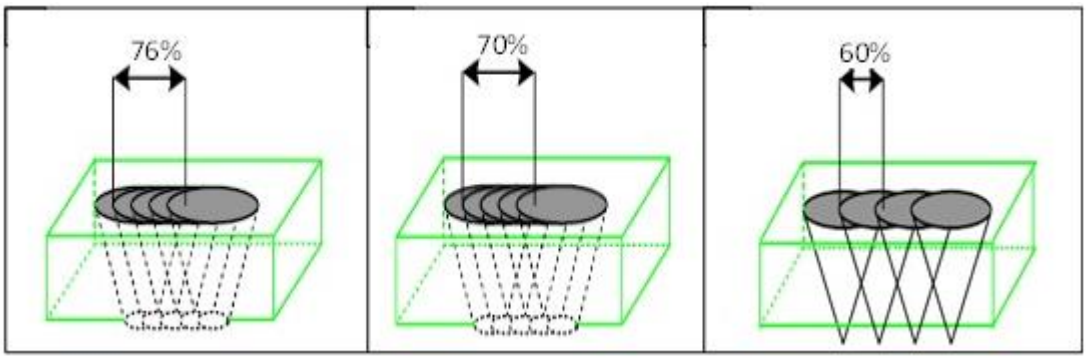

(a) (b) (c)

Figure 5. Surface and depth of the keyhole affected by laser beam overlapping (Q_f) of: (a) 76%, (b) 70% and (c) 60%.

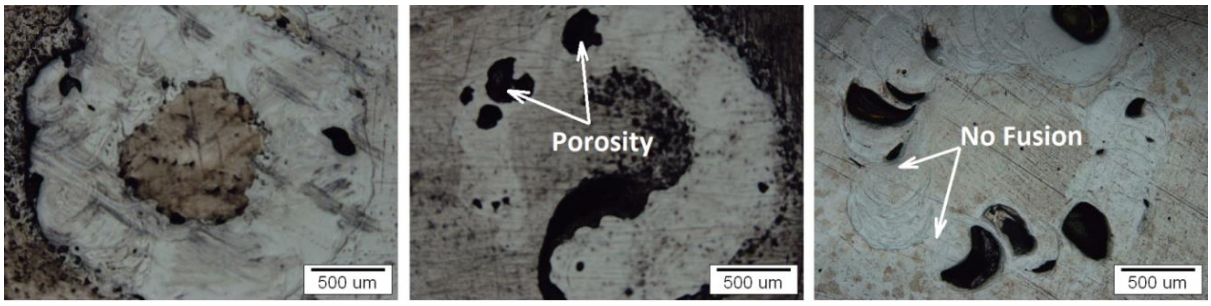

(a) (b) (c)

Figure 6. Images of fused areas at bottom of Ti sheet for different overlapping factor (O_f) values: (a) 76%, (b) 70% and (c) 60%.

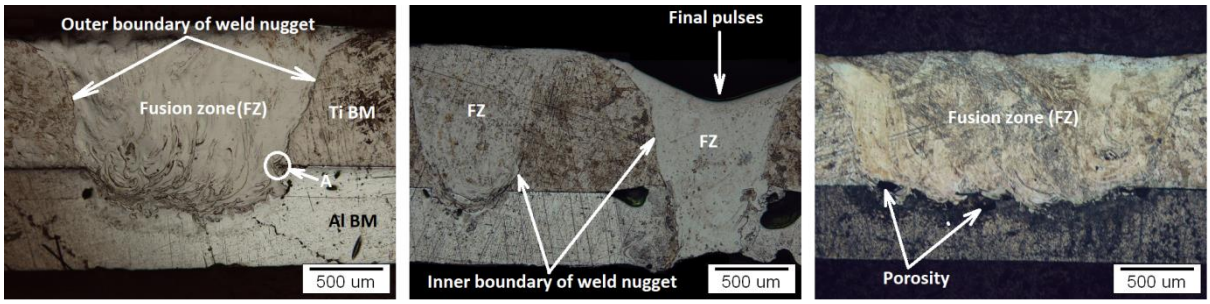

(a) (b) (c)

Figure 7. Cross sections of the weld strips highlighted in Figure 3: (a) Section 1, (b) Section 2 and (c) Section 3.

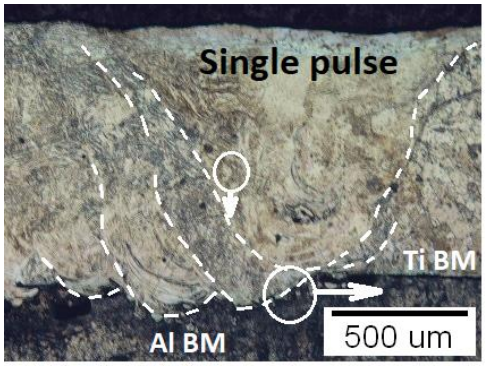

(a)

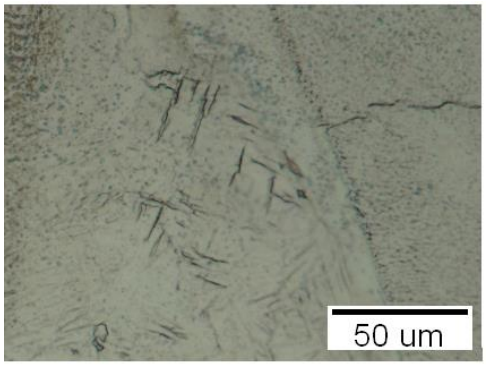

(b)

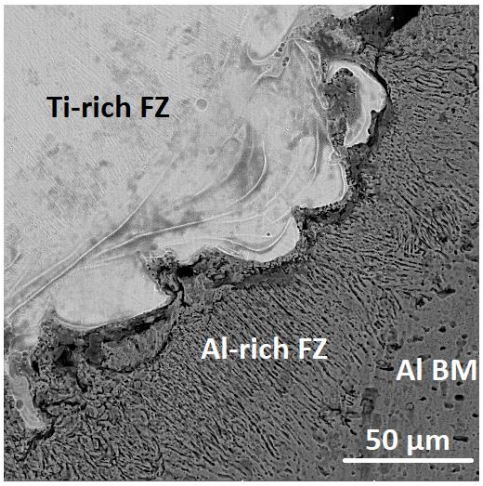

(c)

Figure 8. Microstructure of sample 3 (V = 6.67 mm.s^{-1}); (a) serrated α grains in fusion zone of a single pulse, (b) acicular ά martensite in Ti fusion zone, and (c) Al base-metal/fusion zone interface.

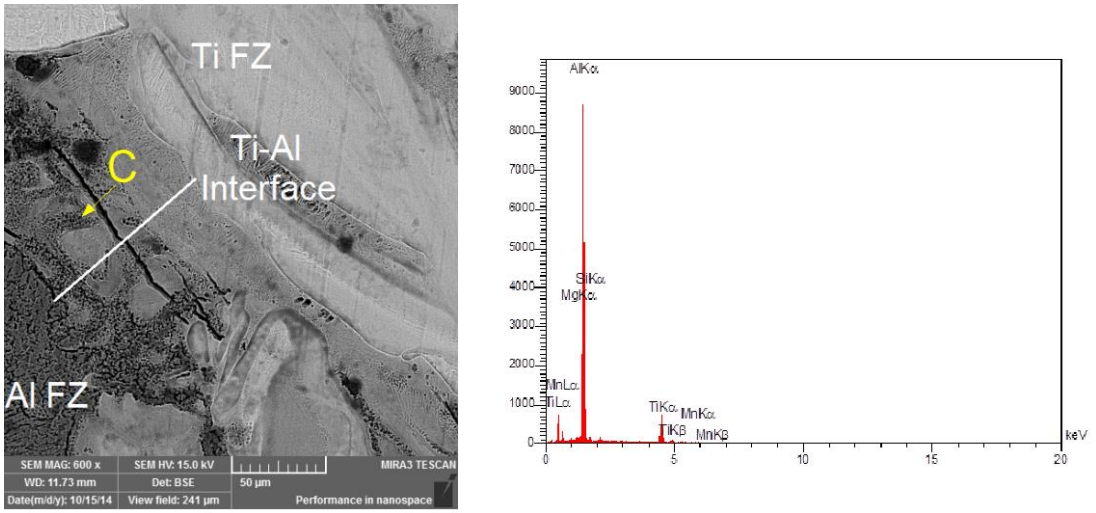

(a) (b)

Figure 9. Cracks near the Ti-Al interface at welding speed of 5 mm.s^{-1}: (a) SEM image and (b) EDS result.

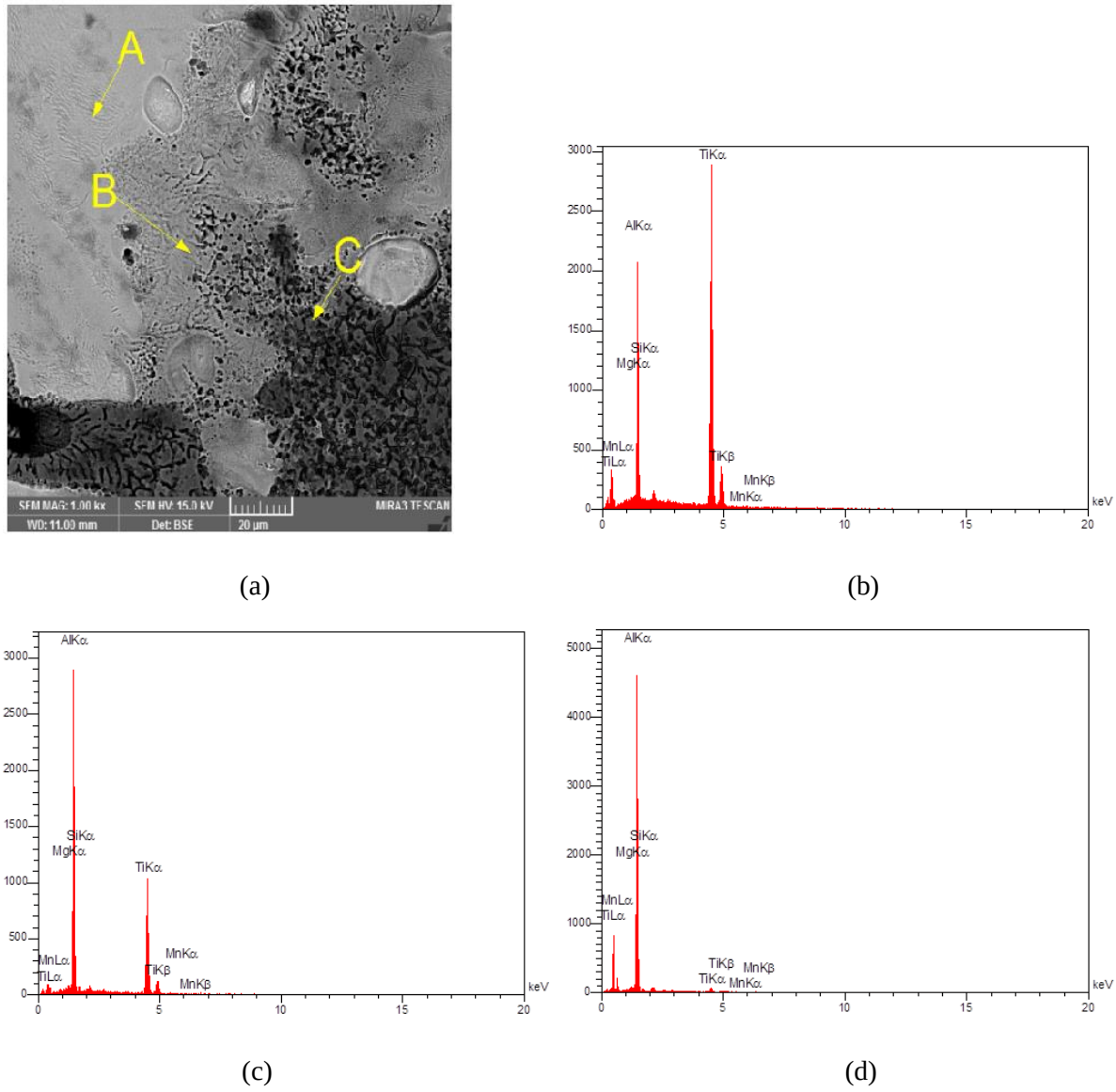

Figure 10. Microstructures of zone A of Figure 7a and its adjacent regions: (a) SEM image for zone A, and (b, c and d) EDS pattern of points A, B, and C of part (a), respectively.

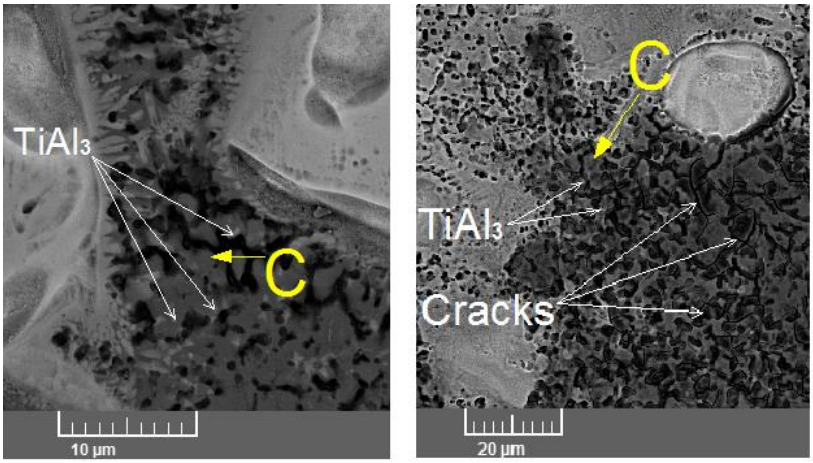

(a) (b)

Figure 11. SEM image nearby the point C at the welding speed of: (a) 6.67 and (b) 4 $mm.s^{-1}$.

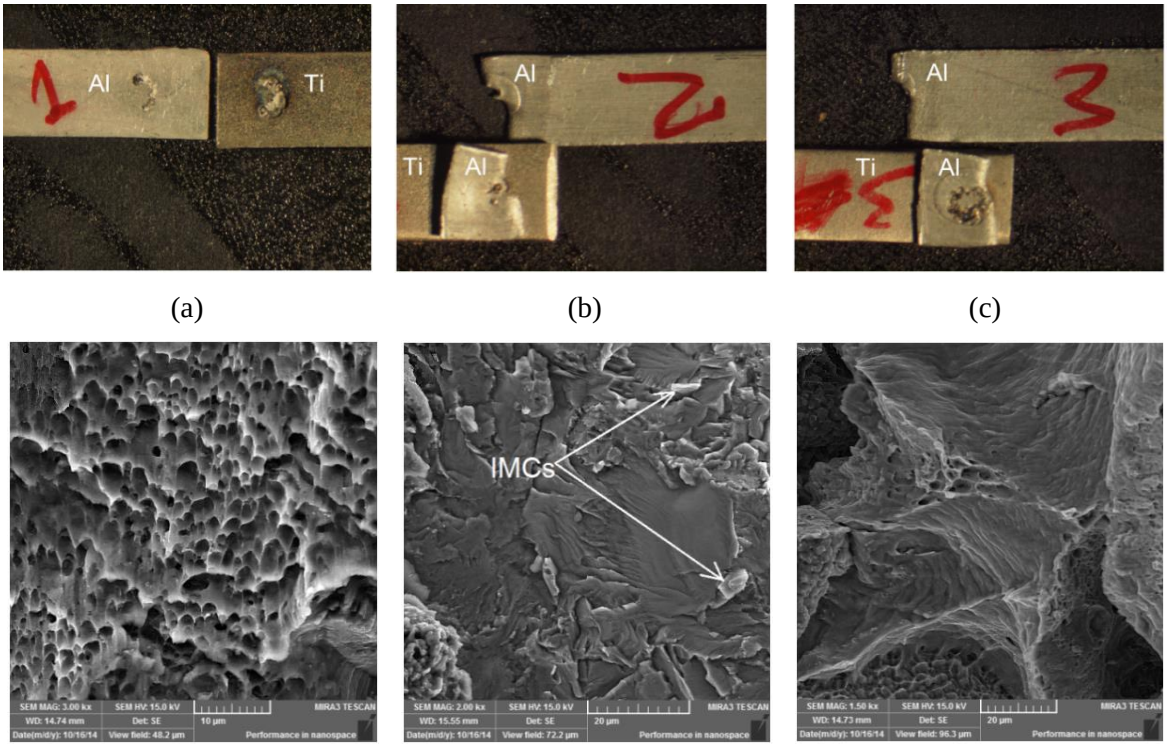

(a) (b) (c)

(d) (e) (f)

Figure 12. Optical (a, b, and c) and SEM (d, e, and f) images of the samples fractured under shear load at welding speed of: (a,d) 6.67, (b,e) 5, and (c,f) 4 $mm.s^{-1}$.

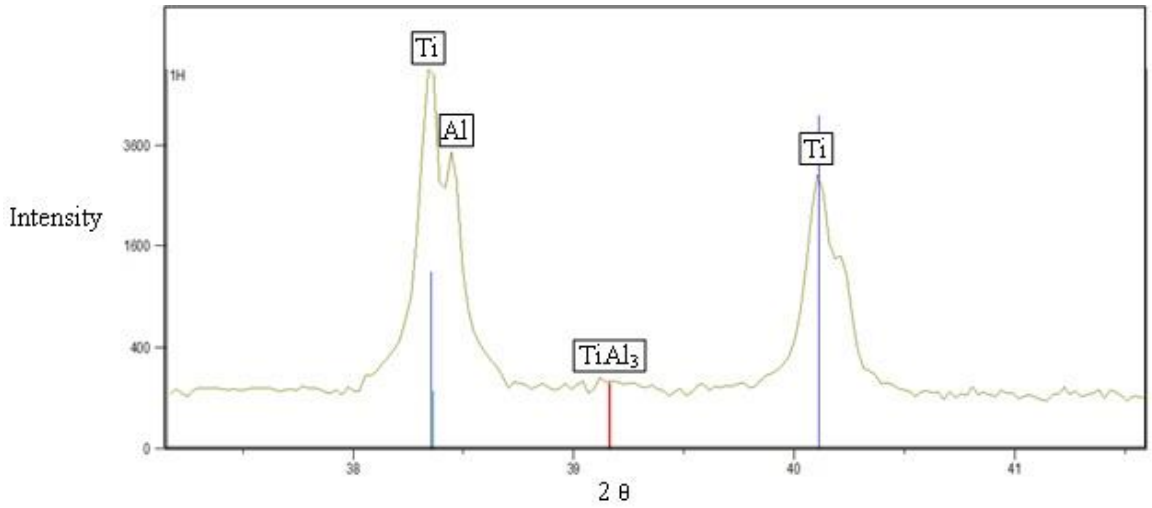

Figure 13. XRD patterns at the fracture interface of Ti shown in Figure 12e.

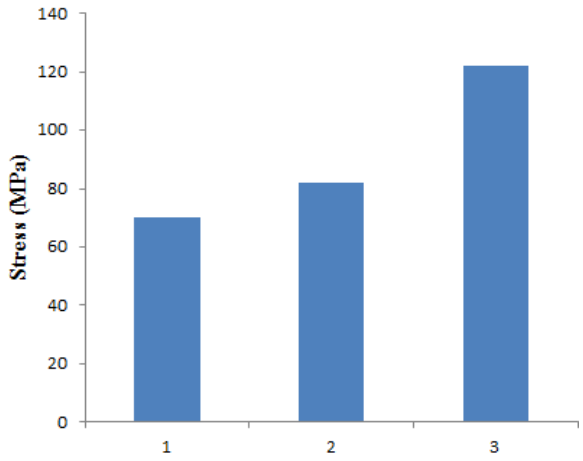

Figure 14. Values of: (1) the shear stress for the joint welded at 4 mm.s^{-1} (76% pulses overlap), (2) the shear stress for the Al base-metal, and (3) the tensile stress for Al base-metal.

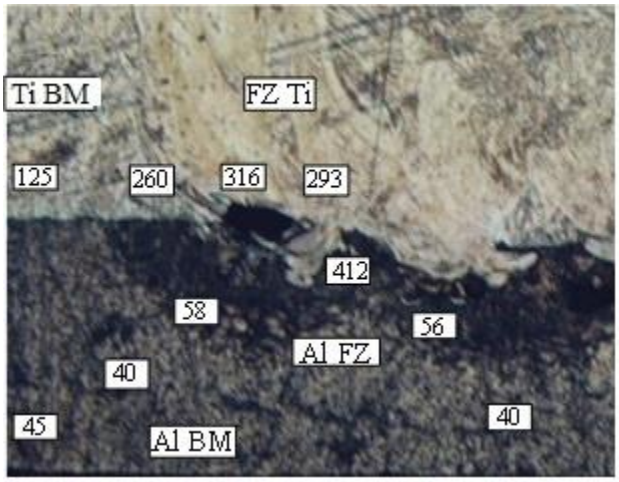

(a)

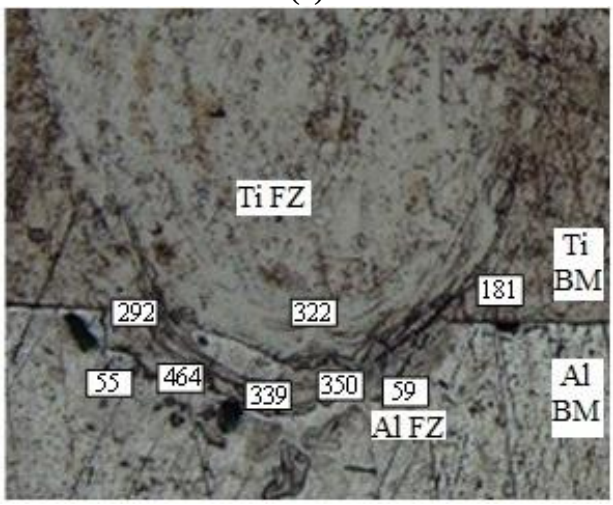

(b)

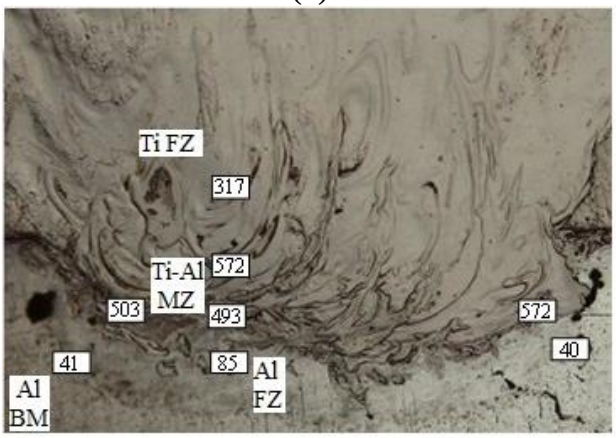

(c)

Figure 15. Base-metal (BM), Fusion Zone (FZ) and Mixing Zone (MZ) microhardness measurement locations on the Ti-Al couple welded at the speed of: (a) 6.76, (b) 5 and (c) 4 mm.s^{-1}.